Multispectral and Hyperspectral Remote Sensing of Alpine Snow Properties

Jeff Dozier

*Donald Bren School of Environmental Science and Management, University of California,
Santa Barbara, California 93106; email: dozier@bren.ucsb.edu*

Thomas H. Painter

*National Snow and Ice Data Center, University of Colorado, Boulder,
Colorado 80309; email: tpainter@nsidc.org*

Key Words snowmelt, albedo, snow-covered area, reflectance, grain size

■ **Abstract** Models of processes in the alpine snow cover fundamentally depend on the spatial distribution of the surface energy balance over areas where topographic variability causes huge differences in the incoming solar radiation and in snow depth because of redistribution by wind. At a spatial scale commensurate with that of the terrain, we want to know which areas are covered by snow, and we want to estimate the snow's spectral albedo, along with other properties such as grain size, contaminants, temperature, liquid water content, and depth or water equivalent. From multispectral and hyperspectral remote sensing at wavelengths from 0.4–15 μm, the retrievable properties include snow-covered area, albedo, grain size, liquid water very near the surface, and temperature. Spectral mixture analysis allows the retrieval of the subpixel variability of snow-covered area, along with the snow's albedo. Remaining research challenges include the remote sensing of absorbing impurities; accounting for variability in the bidirectional-reflectance distribution function and the variability of grain size with depth; retrieving snow cover in forested regions; reconciling field measurements of emissivity with snow properties; and adapting the algorithms to frequent, large-scale processing.

INTRODUCTION

Midlatitude alpine snow cover and its subsequent melt can dominate local to regional climate and hydrology in the world's mountainous regions. Spatially explicit models of snowpack dynamics and snowmelt (Kirnbauer et al. 1994; Cline et al. 1998; Luce et al. 1998, 1999; Colee et al. 2000) require field data and remotely sensed imagery for initialization, calibration, and validation. Field measurements are sparse or infrequent and subject to disagreeable conditions or avalanche danger in many environments. Subject to availability of instrument duty cycles and constrained by cloud cover, remote sensing techniques can regularly and safely

465

provide maps of snow properties for the model domain at a range of resolutions. Some measurements are possible with multispectral sensors, i.e., those with several or more discrete wavelength bands. Other measurements require hyperspectral remote sensors, typically with 100–200 contiguous wavelength channels.

Distributed snow-surface energy-balance models need the following spatially distributed parameters: snow-covered area; albedo; grain size; snow water equivalent; snow temperature profile; and meteorological conditions, including radiation. With additional information about snowpack layers, energy-balance models can be coupled to calculations of meltwater flux or snow metamorphism. In the visible and near-infrared portions of the electromagnetic spectrum, we can directly estimate snow-covered area and grain size, from which we can calculate albedo. In the infrared, we can measure surface temperature.

To the extent possible, remote sensing of snow properties derives from first principles about the optical properties of snow. Radiative transfer models of snow reflectance and transmittance treat the snow grains as independent scatterers because the grain sizes and their center-to-center separations are much larger than the wavelength of the light. Because of multiple scattering as light enters the snowpack, penetration depths are restricted to no more than 0.5 m in the blue wavelengths and are only a few millimeters in the near-infrared and infrared. Therefore, the possibility of remotely sensing snow water equivalent is severely limited, and one must use active microwave remote sensing to measure this important variable in alpine regions (Shi & Dozier 2000a,b). In areas where spatial resolution is not an issue, passive microwave remote sensing can estimate snow water equivalent at values well below 1 m, where the signal becomes asymptotic (Goodison & Walker 1994, Foster et al. 1997, Chen et al. 2001). Remaining parameters come from a combination of in situ measurements and terrain-based energy-balance models (Dozier & Frew 1990, Daly et al. 2000, Davis et al. 2001).

OPTICAL PROPERTIES OF ICE AND SNOW

A scattering model for any granular medium has two sets of input parameters: the wavelength-dependent complex index of refraction of the constituent materials, and the distribution of the sizes and shapes of the grains. In the case of snow, there are three possible constituents: ice, liquid water, and absorbing impurities such as dust or soot.

Figure 1 shows the complex refractive index $N = n + ik$ for ice and water over the wavelengths of the solar spectrum at Earth's surface, 0.4–2.5 μm, covering the wavelength range of most instruments that measure the reflected signal. The real part $n = c_0/c$ is the ratio of the speed of light in vacuum to that in the medium. The imaginary part k, also called the absorption coefficient, is defined by $dI/I = -(4\pi k/\lambda)dx$, describing how radiation of intensity I at wavelength λ decays as it passes along distance x through a pure medium. There is little spectral variability in the real part n, enough to cause a rainbow, but the absorption coefficient k varies by seven orders of magnitude over the visible and near-infrared wavelengths.
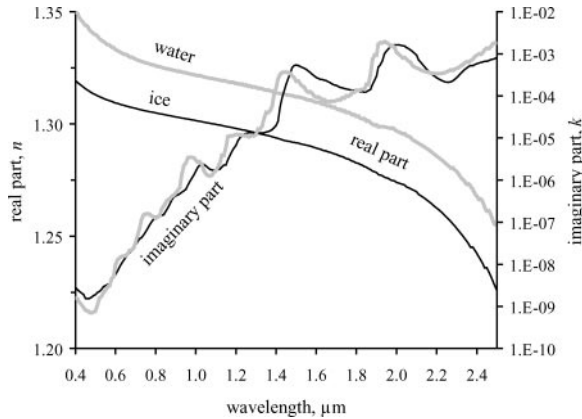
Figure 1 Complex refractive indices of ice and water
(Wiscombe 1994, 1995).

Figure 2 shows the spectral reflectance of snow (Wiscombe & Warren 1980)
for varying grain radii, along with the absorption coefficient k expressed as an
e-folding distance, at which the intensity of the radiation passing through a pure
medium is reduced by e^{-1}. In wavelengths where ice is either highly transparent
or nearly opaque, the reflectance of snow is insensitive to grain size. For example,
at $\lambda = 0.46 \ \mu$m, the e-folding distance in ice is 24 m, so increasing the size of
a grain of snow does not appreciably increase the probability that a photon will
be absorbed while passing through it. Similarly, at 1.6 μm, the e-folding distance
is approximately 0.3 mm, so snow will be dark unless the grain sizes are very
small.

There is little difference between the absorption coefficients for ice and water;
the absorption features of ice mimic those of water with a slight shift toward
longer wavelengths. The main effect of liquid water in snow is that it causes the
grains to form clusters (Colbeck 1979), which behave optically as large grains,
so reflectance in the near-infrared decreases when the snow is wet because of
the clusters and not because of liquid water per se. When wet snow refreezes,
the near-infrared reflectance remains depressed (O'Brien & Munis 1975). With a
hyperspectral sensor, it is possible to estimate the liquid water fraction near the
snow surface by examining the wavelengths where there is a slight shift in the
absorption coefficient of ice versus water (Green et al. 2002).

Absorbing impurities affect the reflectance only in the visible wavelengths
(Warren & Wiscombe 1980), where there is a huge difference between the absorp-
tion coefficient of ice ($\sim 10^{-8}$) and soot or dust (0.001–1.0).

The depth of the snowpack (or the snow water equivalent, which is depth $\times$
density) affects the reflectance only for shallow snow and only in the visible part of
the spectrum. In the near-infrared, the snow is effectively semi-infinite when depth
exceeds approximately 3 cm, whereas in the visible wavelengths the semi-infinite
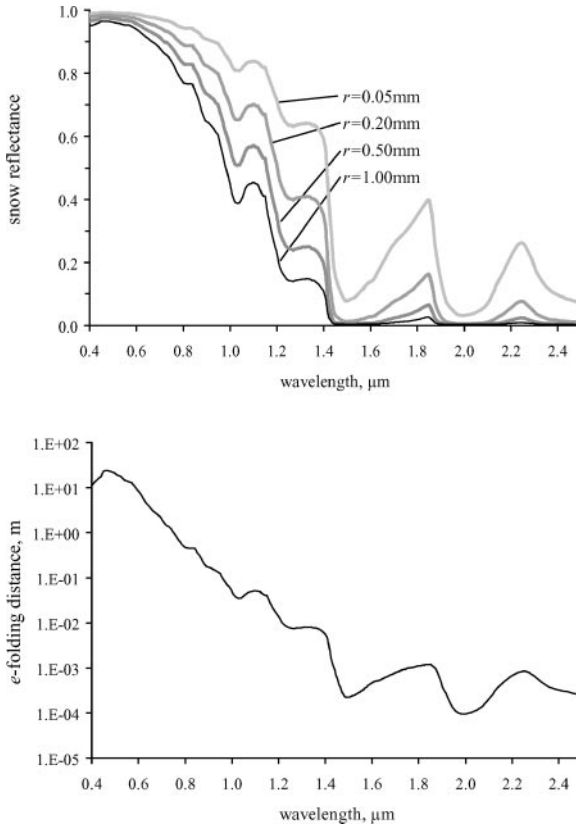
Figure 2 Spectral reflectance of pure snow of varying grain radii (using the model of Wiscombe & Warren 1980) showing the relationship between reflectance and the absorption coefficient of ice, expressed as the *e*-folding distance.

depth is as large as 50 cm, depending on grain size and density, but the top 5–10 cm have the greatest effect on the signal (Zhou et al. 2004).

In the infrared part of the spectrum, ice is highly absorptive. Snow emissivity variations caused by density, grain shape, liquid water, and grain size are apparently unimportant, but at highly off-vertical viewing angles, emissivity varies enough to produce differences between thermodynamic temperature and brightness temperature as large as 3 K at wavelengths 12–14 μm, which is at the outer edge of the major atmospheric infrared window (Dozier & Warren 1982).

Given the optical properties of ice, the scattering properties of a grain are calculated with Mie theory (Wiscombe 1980, Nussenzveig & Wiscombe 1991). The multiple scattering properties of a snowpack are then calculated with the radiative transfer equation. A two-stream approximation (Meador & Weaver 1980) computes only the angularly integrated reflectance, but has an analytic solution

for many applications. A more complicated, more accurate model, e.g., DISORT
(Stamnes et al. 1988, Thomas & Stamnes 1999), yields the angular distribution of
spectral reflected intensity as well, i.e.,

$$R_\lambda(\theta_0, \phi_0; \theta_r, \phi_r) = \pi f_{r\lambda}\left(\theta_0, \phi_0; \theta_r, \phi_r; \frac{E_{\lambda,\text{diffuse}}}{\mu_0 E_{\lambda,\text{direct}} + E_{\lambda,\text{diffuse}}}\right)$$

$$= \frac{\pi L_\lambda(\theta_r, \phi_r)}{\cos\theta_0 E_{\lambda,\text{direct}}(\theta_0, \phi_0) + E_{\lambda,\text{diffuse}}}. \tag{1}$$

$f_{r,\lambda}$ is the hemispherical-directional reflectance distribution function, θ and ϕ are
zenith and azimuth angles, and the subscripts 0 and r signify incident and reflected.
L_λ is reflected radiance, $E_{\lambda,\text{direct}}$ is the direct incident irradiance on a surface normal
to the beam, and $E_{\lambda,\text{diffuse}}$ is the diffuse incident irradiance. The spectral albedo is
the value of R_λ in Equation 1 integrated over the upward-looking hemisphere.

A measurement of effective grain size is needed for the Mie scattering calcula-
tions. Normally, examiners of snow grains in the field characterize the grains by
choosing the largest dimension. However, the effective grain radius for radiative
transfer applications is smaller. The radius of the sphere with the same surface-
to-volume ratio of the actual grains represents many of the snow's characteristics
adequately (Warren 1982). This ratio can be measured with stereological methods
in a cold laboratory (Dozier et al. 1987) or estimated in the field by characterizing
the smaller dimensions of a grain. To account for size heterogeneity and nonspher-
ical shapes, one can use a spatial autocorrelation function to represent an effective
size (Mätzler 1997), or one may model a nonspherical shape as a collection of
spheres (Grenfell & Warren 1999). The use of an effective spherical grain size is
adequate for calculations of spectral albedo, but more complicated grain shapes
require consideration when the angular details of the reflectance are needed.

REMOTE SENSING OF SNOW-COVERED AREA

For three decades, satellite remote sensing instruments have measured snow prop-
erties from drainage-basin to continental scales (Hall & Martinec 1985). Snow-
covered areas, derived from multispectral measurements in the visible and near-
infrared parts of the spectrum, were among the earliest geophysical measurements
from satellites (Rango & Itten 1976), and the measurements were soon incorpo-
rated into snowmelt-runoff models (Rango & Martinec 1979, Rango & Shalaby
1998). The earliest remote sensing of snow properties focused primarily on map-
ping the snow extent with multispectral sensors, such as the Landsat Multispectral
Scanning Subsystem (MSS), the Landsat Thematic Mapper (TM), and the NOAA
Advanced Very High Resolution Radiometer (AVHRR). Going beyond measure-
ments of snow extent, Dozier et al. (1981) applied a snow reflectance model
(Wiscombe & Warren 1980) to remote sensing of snow properties with the AVHRR,
and they were able to detect a growth in grain size and a decrease in snow water

equivalent on snow-covered lakes in Canada. The decrease in snow water equivalent caused the visible reflectance to decrease but did not affect the near-infrared reflectance, whereas the grain growth caused the near-infrared reflectance to drop.

Dozier (1989) proposed a suite of normalized band differences for mapping snow and qualitative grain size with TM data, and most current multispectral schemes for binary mapping of snow cover, by which each pixel is classified as either "snow" or "not snow," are derived from his method. For example, the current scheme in NASA's Earth Observing System (EOS) applies this method to the MODIS (Moderate-Resolution Imaging Spectrometer) instrument for its standard snow map product (Hall et al. 1995, 2002). A normalized difference snow index (NDSI) is calculated from reflectance in bands at wavelengths where snow is bright (e.g., TM band 2 or MODIS band 1) and where it is dark (e.g., TM band 5 or MODIS band 6), along with a band used for threshold brightness (e.g., TM band 4 or MODIS band 2):

$$NDSI = \frac{TM_{band2} - TM_{band5}}{TM_{band2} + TM_{band5}}. \tag{2}$$

A pixel in a clear area is mapped as snow covered when NSDI > 0.4 and $TM_{band4} >$ 0.11. In a forested area, the pixel is mapped as snow when $0.1 <$ NSDI < 0.4.

Common Multispectral Instruments

In all snow products, and in remote sensing in general, there is a tradeoff between spatial resolution and swath width (and thus frequency of observations). Because most hydrologic applications require regular, frequent measurements, the instruments that provide the bulk of the data used have been NOAA/AVHRR and EOS/MODIS in the optical part of the spectrum, with spatial resolutions of 1.09 km and 500 m at nadir. These data are available daily, whereas finer-resolution instruments like the Landsat TM have 30-m spatial resolution but a 16-d repeat cycle.

The Landsat satellites began flying in 1972 (NASA 1999). Through 1983, Landsats 1–3 carried the MSS, whose wavelength characteristics are in Table 1. With 79 m ground resolution [more properly, ground instantaneous field-of-view (IFOV)] and a 185 km swath, Landsats 1–3 had an 18 d repeat cycle. In 1982,

TABLE 1   MSS wavelengths on Landsats 1–5 (NASA 1999)

Band No.			
Landsat 1–3	Landsat 4–5	Wavelength range (μm)	Ground IFOV (m)
4	1	0.5–0.6	79
5	2	0.6–0.7	79
6	3	0.7–0.8	79
7	4	0.8–1.1	79
8		10.41–12.6	237

TABLE 2   TM wavelengths on Landsats 4 and 5 (NASA 1999)

Band No.	Wavelength range (μm)	Ground IFOV (m)
1	0.45–0.53	30
2	0.52–0.60	30
3	0.63–0.69	30
4	0.76–0.90	30
5	1.55–1.75	30
6	10.40–12.50	120
7	2.08–2.35	30

Landsat 4 was launched with the TM with seven spectral bands (Table 2), a more versatile instrument than the MSS, with 30-m ground IFOV and a 16 d repeat cycle. Landsats 4 and 5 carried the MSS as well as the TM. Landsat 6 failed at launch, and Landsat 7 was launched in 1999 with the Enhanced Thematic Mapper (ETM+; Table 3), which included a 15 m–resolution panchromatic band in addition to those on the TM.

The AVHRR provides four- to six-band multispectral data from the NOAA polar-orbiting satellite series (USGS 2003). There is fairly continuous global coverage starting with NOAA-6 in June 1979, with morning and afternoon acquisitions available. The wide swath enables daily global coverage from each satellite. Table 4 shows the spectral characteristics of the bands. The original four-band instrument had bands 1, 2, 3B, and 4 for cloud and surface mapping and sea-surface temperature. Band 5 was added to improve atmospheric correction for sea-surface temperature during the daytime. On the six-band instrument that first flew on NOAA-16 in 2000, band 3A was added for snow/cloud discrimination.

Terra (NASA/GSFC 2003b), the flagship of NASA's EOS, was launched in 1999 with three instruments used for snow mapping: MODIS, MISR (Multi-angle

TABLE 3   ETM+ wavelengths on Landsat 7 (NASA 1999)

Band No.	Wavelength range (μm)	Ground IFOV (m)
1	0.45–0.515	30
2	0.525–0.605	30
3	0.63–0.69	30
4	0.75–0.90	30
5	1.55–1.75	30
6	10.40–12.50	60
7	2.09–2.35	30
Pan	0.52–0.90	15

TABLE 4   AVHRR wavelengths on the NOAA meteorological satellites
(NOAASIS Gateway 2003)

Band No.	Wavelength range (μm)	Ground IFOV (km)
1	0.58–0.68	1.09
2	0.725–1.00	1.09
3A	1.58–1.64	1.09
3B	3.55–3.93	1.09
4	10.30–11.30	1.09
5	11.50–12.50	1.09

Imaging SpectroRadiometer), and ASTER (Advanced Spaceborne Thermal Emission and Reflection Radiometer). Terra is in sun-synchronous orbit with a morning equator-crossing time, so each image at a specific location occurs at the same local time. Its companion, Aqua (NASA/GSFC 2003a), launched in 2002 in sun-synchronous orbit with an afternoon equator-crossing time, also carries MODIS.

MODIS has 36 bands with spatial resolutions varying from 250 m (2 bands), 500 m (5 bands), to 1 km (29 bands). Table 5 shows the bands used for land applications. The MODIS snow algorithm (Hall et al. 2002) applies Equation 2 using bands 1, 2, and 6.

MISR (JPL MISR Team 2003) exploits angular information in the signal for study of surface bidirectional reflectance and for information about aerosols by observing the surface at different path lengths through the atmosphere. It has four spectral bands (blue, green, red, near-infrared), nine camera angles ($0°$, $\pm26.1°$, $\pm45.6°$, $\pm60.0°$, $\pm70.5°$), and achieves global coverage in two to nine days depending on latitude. Its primary uses for snow are measurement of albedo (Stroeve & Nolin 2002) and estimation of snow cover under a forest canopy.

ASTER (JPL ASTER Team 2003) exploits the signal from both reflected and emitted radiation. It has 15 bands, 4 in the visible/near-infrared with spatial

TABLE 5   MODIS bands for land applications (NASA MODIS Team 2003)

Band No.	Wavelength range (μm)	Ground IFOV (m)
1	0.620–0.670	250
2	0.841–0.876	250
3	0.459–0.479	500
4	0.545–0.565	500
5	1.230–1.250	500
6	1.628–1.652	500
7	2.105–2.155	500

TABLE 6   POLDER bands (CNES POLDER Team 2003b)

Band No.	Wavelength range (μm)	Polarized
443P	0.4345–0.4545	Yes
443NP	0.4349–0.4549	No
490NP	0.4822–0.5022	No
565NP	0.5545–0.5745	No
670P	0.6602–0.6802	Yes
763NP	0.7583–0.7683	No
765NP	0.7431–0.7831	No
910NP	0.8977–0.9177	No
865P	0.8408–0.8808	Yes

resolution of 15 m, 6 in the shortwave infrared (1.60–2.43 μm) with spatial resolution of 30 m, and 5 in the thermal infrared (8.125–11.65 μm) with spatial resolution of 90 m. ASTER has the bands capable of mapping subpixel snow and grain size (Shi 1999), with coregistered temperature, but the applications published so far address glacier mapping and inventory (Raup et al. 2000, Kaab 2002).

POLDER (POLarization and Directionality of the Earth's Reflectances) is a wide FOV imaging radiometer that has provided global, systematic measurements of spectral, directional, and polarized characteristics of the solar radiation reflected by Earth and its atmosphere (CNES POLDER Team 2003a). Launched first in 1996 on the Japanese ADEOS (Advanced Earth Observing Satellite), it collected data for eight months. It was also launched in December 2002 on ADEOS-2, which failed with an operational anomaly in October 2003. With nine bands, some with polarization (Table 6), POLDER exploited information about polarized reflectance from Earth's surface and atmosphere. Its large pixel size (6 $\times$ 7 km) limited its utility for snow mapping in alpine regions, but it collected some unique data about the polarized bidirectional reflectance from Antarctica (Mondet & Fily 1999).

Hyperspectral Instruments

AVIRIS (Airborne Visible/Infrared Imaging Spectrometer) measures reflected radiance in the wavelength range 0.4–2.5 μm with 0.01-μm spectral resolution. It uses 4 spectrometers, and has 224 spectral bands. Normally flying on the ER-2 aircraft at a height of 20 km, it has a nominal spatial resolution of 20 m, varying with the elevation of the surface, and a 15° scan angle on either side of nadir (JPL AVIRIS Team 2003). AVIRIS also flies on a Twin Otter at much lower altitude, where it can obtain spatial resolution in the 1–2 m range. AVIRIS has been the data source for almost all published hyperspectral investigations of snow.

Hyperion is a spaceborne hyperspectral imager with 220 spectral bands (0.4–2.5 μm) and a 30-m spatial resolution (NASA/GSFC EO-1 Team 2003). The instrument images a 7.5 $\times$ 100 km land area per image and provides detailed spectral mapping across all 220 channels with high radiometric accuracy. A search of the journal and conference literature uncovers no published papers on snow mapping yet, but an abstract has been published on mapping grain size and albedo in Greenland (Nolin et al. 2001), and a Hyperion data set is available for NASA's Cold Land Processes Experiment (Painter 2002a).

The Need for Snow Mapping at Subpixel Resolution

Snow-covered area in alpine terrain often varies at a spatial scale finer than that of the ground IFOV of the remote sensing instrument. This spatial heterogeneity poses a mixed pixel problem in that the sensor may measure radiance reflected from snow, rock, soil, and vegetation. To use the snow characteristics in distributed physical models, we must therefore map snow-covered area at subpixel resolution in order to accurately represent its spatial distribution; otherwise, systematic errors may result.

The MODIS algorithm, for example, identifies pixels whose snow cover fraction is greater than approximately 50% as entirely snow-covered, whereas those pixels where the snow-cover fraction is less than 50% are mapped as snow-free (the algorithm can be tuned to adjust these thresholds). One could assume that, on average, overestimates will balance underestimates, and perhaps for some applications this assumption is correct. However, consider Figure 3. Two simulated MODIS images (500-m pixel size) were created from AVIRIS data (17-m pixel size), one with a continuous snow distribution and the other with a patchy snow distribution.
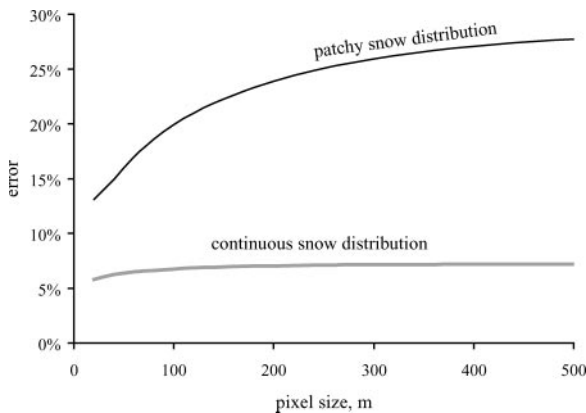

Figure 3 Effect of the characteristics of the snow distribution on the standard MODIS algorithm performance at different resolutions for patchy and continuous snow distributions, compared to fine-resolution aerial photographs (J. Shi, personal communication).

The relative error compares the snow cover derived from high-resolution visible and near-infrared color photos (1–4-m pixel size) and that derived from the current MODIS algorithm (J. Shi, personal communication). The snow's spatial distribution has significant impact on the algorithm's accuracy. For the patchy snow distribution case, the accuracy decreases significantly as the ground IFOV increases because of the mixed-pixel problem. Even for the continuous snow distribution case, ignoring subpixel variability introduces systematic error. The straightforward application of an algorithm derived from TM data with 30 m resolution (Dozier 1989) would be expected to yield different results when applied to coarser-resolution data. A snowmelt model will not realistically average out this kind of error.

Spectral Mixture Analysis

Spectral mixture analysis is a method of inverting multispectral or hyperspectral data to enable mapping land cover at subpixel scale (Adams et al. 1993, Mertes et al. 1993, Roberts et al. 1998, Okin et al. 2001). Linear spectral mixture analysis is based on the assumption that the radiance measured at the sensor is a linear combination of radiances reflected from individual surfaces, endmembers, whose spectral signatures are unique and well separated above a random image noise level (Sabol et al. 1992). The linear assumption is appropriate for spatial scenarios such as snow and rock cover above timberline where the surface is near planar. Nonlinear analysis, which accounts for multiple scattering between surfaces, is necessary when the surface has a structure such as vegetation that reflects and transmits radiation to the snow or soil substrate and other vegetation (Roberts et al. 1993). Vegetation above the snow surface occludes viewing the complete snow cover, so below timberline, the measures of subpixel snow-covered area represent the viewable snow cover through the vegetation canopy gaps. Soon after snow storms, the projected snow-covered area includes snow intercepted by the canopy, which is indistinguishable from snow on the ground at resolutions coarser than the footprint of a tree. In some climates, snow may remain in the canopy for weeks.

The analysis is based on a set of simultaneous linear equations, one for each wavelength band λ:

$$R_{S,\lambda} = \sum_{i=1}^{M} F_i R_{\lambda,i} + \varepsilon_\lambda. \tag{3}$$

F_i is the fraction of endmember i, $R_{\lambda,i}$ is the reflectance (more properly, the hemispherical-directional reflectance factor) of endmember i at wavelength λ, M is the number of spectral endmembers, and ε_λ is the residual error at λ for the fit of the M endmembers (Gillespie et al. 1990). The values for F_i can be found from some numerical scheme that minimizes the sum of squares of the residual errors (Golub & Van Loan 1996). Analysis of residuals reveals the spectral regions of poor modeling and can be useful for separating materials with similar spectral reflectances (Roberts et al. 1993).

Spectral mixture analysis has been used for snow mapping with both multi-spectral and hyperspectral instruments. Generally, the hyperspectral instruments provide sufficient data to enable mapping not only of snow cover but of other properties as well, whereas the multispectral instruments have data sufficient only to map snow, although more robust mapping from multispectral data is a focus of current research. Nolin et al. (1993) first demonstrated spectral mixture analysis for subpixel snow-cover mapping, using the hyperspectral aircraft instrument AVIRIS. They modeled two AVIRIS datasets with single endmember suites of (*a*) snow, rock/soil, water, and vegetation and (*b*) snow, shade, and vegetation. The spectral band subset consisted of 18 bands: 3 in visible wavelengths (0.46, 0.55, 0.66 μm), 3 in the near-infrared (0.72, 0.85, 0.94 μm), and 12 bands spanning the 1.03 μm ice absorption feature.

Rosenthal & Dozier (1996) developed linear spectral mixture analysis for sub-pixel snow-covered area from Landsat TM. Although the use of Landsat gave up the advantages of rich hyperspectral data, they were able to map snow over entire Landsat swaths several times during a season. Validation of their method with high-resolution (0.6 m) aerial photography demonstrated accuracy equal to that obtainable from the aerial photographs, but over a vastly larger area. The mapping method is insensitive to the choice of lithologic or vegetation endmembers, the water equivalent of the snow pack, snow grain size, or local illumination angle.

The Landsat spectral mixing model can also be used to map snow on glaciers. Thought to be sensitive indicators of climatic variability, the tropical glaciers in the central Andes are presently in a state of rapid retreat. Klein & Isacks (1999) applied Landsat TM spectral mixture analysis to identify the ablation and accumulation zones and the transient snowline on the Zongo Glacier in the Cordillera Real, Bolivia, and the Quelccaya Ice Cap in Peru, and found the method more effective than single bands or band ratios in discriminating the accumulation and ablation zones on these small tropical glaciers.

Forests represent a challenging problem for snow-cover mapping by multi-spectral or hyperspectral remote sensing because of the difficulty in seeing snow underneath a canopy and because the brightness of snow in the shadow of a tree is less than in sunlight. Vikhamar & Solberg (2003) applied corrections for the problem of shadowing by trees and mapped snow with Landsat TM in the Jotunheimen region of South Norway. Their results were better for pine forests and mixed pine and birch forests than for thicker spruce forests. Klein et al. (1998) also proposed modifying the standard MODIS algorithm to include a normalized difference vegetation index with the snow index to improve snow mapping in areas of forest cover.

Kaufman et al. (2002b) developed a statistical method for mapping subpixel snow cover using only two MODIS bands at 0.66 and 2.1 μm. Their analysis showed good agreement with one image classified with the Rosenthal & Dozier (1996) method. If this agreement holds over a wide range of conditions, it could be used for global mapping. The question that remains is whether it is robust,

independent of whether the nonsnow fraction of the pixel is mainly soil or vegetation (Jin et al. 2002).

Figure 4 shows a calculation of subpixel snow cover from MODIS data (using an algorithm adapted to MODIS data from Painter et al. 2003). Comparison with the standard MODIS mapping reveals both overestimates and underestimates of snow cover.

REMOTE SENSING OF OTHER PROPERTIES

Grain Size and Albedo

Models of the surface energy balance require an estimate of snow albedo, integrated over the solar spectrum and weighted by the spectral solar irradiance. Many hydrologic and climate models treat snow albedo as a constant or a parameter, but measurements always show that it varies both spatially and temporally (Winther 1993). Nolin & Stroeve (1997), for example, observed a 20% decline in albedo in 10 days over a large area of Greenland, and Hall et al. (1992) observed 30% differences between clean and dusty snow. Because few satellite and aircraft instruments measure over the whole spectrum, snow albedo is normally inferred from snow properties such as grain size and contaminants instead of directly measured. Grain size is the snow parameter that determines its spectral albedo in the near-infrared wavelengths, whereas absorbing impurities and, for shallow snow only, snow water equivalent affect its albedo in the visible spectrum (Warren & Wiscombe 1980, Wiscombe & Warren 1980).

Dozier et al. (1981) showed that AVHRR data could qualitatively retrieve both snow grain size and snow water equivalence. Several investigations have demonstrated that grain size can be estimated roughly from Landsat TM data. Dozier & Marks (1987) explored the possibility of mapping the spatial distribution of snow grain size with TM data, arriving at qualitative estimates. Bourdelles & Fily (1993) mapped grain size over Adélie, Antarctica, using TM data interpreted with a two-stream snow reflectance model. Fily et al. (1997) estimated grain size from TM data over the Haute Savoie region of the French Alps using a model for the bidirectional reflectance of snow. The results of these investigations were plausible but they lacked corresponding field measurements of grain size.

Estimates of grain size from Landsat TM rely on bands 4 and 5, which span the wavelength ranges 0.76–0.90 μm and 1.55–1.75 μm, respectively (Table 2). Band 4 is only modestly sensitive to grain size, and snow reflectance in band 5 declines to nearly 0% reflectance once the snow grain radius reaches 250 μm. Therefore, robust remotely sensed measures of grain size are more tractable with an instrument that covers at high spectral resolution the wavelength range 1.0–1.3 μm, where the spectral reflectance of snow is most sensitive to grain size. One method for remotely sensing grain size uses the snow reflectance at 1.03 μm, the wavelength of a prominent ice absorption feature (Nolin et al. 1993). This single-band method is sensitive to sensor noise and requires solid knowledge of the solar and viewing
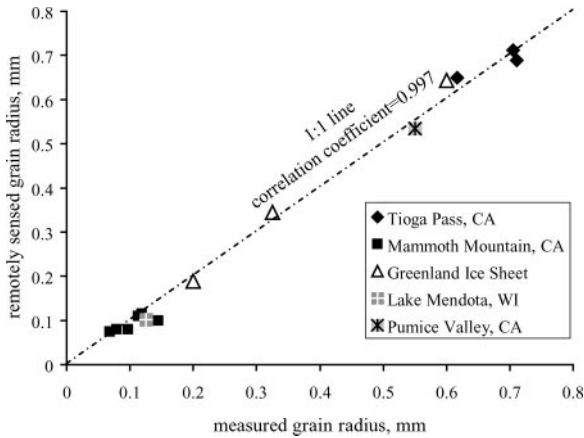
Figure 5   Correlation between snow grain radii measured in the field and inferred from imaging spectrometer data (Nolin & Dozier 2000).

geometry. A subsequent, more robust algorithm (Nolin & Dozier 2000) integrates across the entire 1.03 μm absorption feature, which is scaled spectrally by its continuum. Figure 5 shows good agreement with field measurements under widely different snow and illumination conditions. Li et al. (2001) retrieved grain size from AVIRIS data in a set of specific wavelengths. The value of the grain radius retrieved varied with the wavelength; their interpretation was that grain size varied near the surface, and wavelengths with different penetrations depths therefore see different distributions of grains.

Other investigators have used statistical relationships between satellite- and field-measured albedo (Winther 1992) using a radiometer or spectrometer close to the snow surface. Stroeve & Nolin (2002) estimated snow albedo from the MISR instrument using a correlation between MISR's red channel and field measurements of albedo, and they also incorporated information from MISR's multiangle capability. Comparison with field measurements showed accuracy within 6%, but the absence of a MISR band in the near-infrared where snow albedo is most sensitive to grain size makes this method perhaps site specific. There is no standard EOS snow albedo product, either from MODIS, MISR, or ASTER. A MODIS product is under development, but the prototype has errors as high as 15% (Klein & Stroeve 2002).

With hyperspectral data it is possible to estimate both the fractional snow-covered area and the albedo of that snow. Painter et al. (1998) improved subpixel snow mapping by allowing the spectrum of the snow endmember to vary to match the spectral shape of the pixel's snow reflectance. Because the spectral reflectance of snow decreases with increasing grain size, varying grain sizes in a scene translate into variability of spectral reflectance, and multiple snow endmembers of

different grain sizes are necessary to characterize the snow. Subsequently, Painter et al. (2003) used AVIRIS data to estimate both subpixel snow cover (Figure 6) and grain size (Figure 7) over a wide range of snow conditions in the Sierra Nevada. They validated the measurements of snow area with fine-resolution aerial photographs and the grain-size estimates with stereological analysis of snow samples, i.e., analysis of photographs of planar sections from three-dimensional snow samples (Underwood 1981). Their algorithm uses multiple endmember spectral mixture analysis (Roberts et al. 1998) to simultaneously solve for subpixel snow cover and its grain size. Accuracy of the method was 4% for snow-covered area, 0.048 mm for grain size, and 1.8% for wavelength-integrated albedo.

Liquid Water in Snow

Because of the small penetration distance of light in the wavelengths where the absorption coefficients of ice and water differ, any information about liquid water in snow from multispectral or hyperspectral data is restricted to the near-surface layer. To obtain depth-integrated information about liquid water, one must use active microwave remote sensing (Shi & Dozier 1995a,b).

However, hyperspectral data can provide information about liquid water near the snow surface. In applications of imaging spectrometry to retrieve atmospheric water vapor (Green et al. 1998, Green 2001), the retrieval needs to separate the vapor signal from the liquid signal that may be present in surface vegetation. Similarly, because the absorption features of water and ice are slightly shifted (Figure 1), one can separate all three phases if the spectral information is precise enough. Green et al. (2002) used AVIRIS data to map the solid, liquid, and vapor phases of water by analyzing and distinguishing among the absorption caused by the different phases of water at 0.94 μm (vapor), 0.98 μm (liquid), and 1.03 μm (solid). They quantified the distribution of optical path lengths for ice (related to grain size) and liquid water (related to surface liquid-water content). Figure 8 shows an image of the three phases of water over Mt. Rainier.

Organic and Inorganic Impurities

Warren & Wiscombe (1980) showed that minute concentrations of small highly absorbing particles can lower snow albedo in the visible wavelengths by 5%–15%. Beyond 0.9 μm, however, these particles have no effect on snow albedo because ice itself is more absorptive. Desert dust and carbon soot are the most likely contaminants, from both regional and local sources (e.g., Woo & Dubreuil 1985, Wolff & Cachier 1998), and they can result from both wet and dry deposition (Williams & Melack 1997, Aoki et al. 2000, Meixner et al. 2000). They are present in glacier ice as well. Greuell et al. (2002) used the ratios of TM bands 2 and 4 to estimate broad-band albedo for both snow and ice.

Surprisingly, there seem to be more examples of remote sensing of contaminants in snow on Mars than on Earth (Nolin 1998, Hansen 1999, Bass et al. 2000). Mars'

polar caps are mainly frozen CO_2, but they also contain water ice and dust. Hansen (1999) was able to separate the effects of the contamination. CO_2 snow has a high visible albedo but a low thermal infrared emissivity. Adding water ice does not affect the visible albedo but raises the infrared emissivity, whereas adding dust both lowers the visible albedo and raises the emissivity. Bass et al. (2000) interpreted the summer brightening observed in the north polar cap to be caused by addition of water ice mixed with dust.

The difficulty in remote sensing of absorbing contaminants in snow is that the same aerosols exist in the atmosphere and it is difficult to discriminate between their absorption in the atmosphere and in the snow. Moreover, thin snow also decreases the reflectance in the same wavelength range, visible, as absorbing impurities (Warren 1982). Remote sensing of atmospheric aerosols is one of the key science objectives for the EOS. Over the land surface, the theory of aerosol retrieval from MODIS, which uses a spectral approach, is based on an assumed land reflectance difference between wavelength bands in the blue or red spectrum compared with 2.1 μm (Kaufman et al. 2002a). The validation experiment showed favorable results (Chu et al. 2002), but with a caution about retrieval over snow or ice surfaces. Aerosol retrieval from MISR is based on multiangle observations (Martonchik et al. 1998) and has not been tested over snow or ice surfaces (Martonchik et al. 2002). In areas where the impurity concentration is large because of local sources, the Landsat TM can identify areas where surface concentration is high (Winther 1992). A single experiment that compared hyperspectral data to field-measured impurities showed good agreement between measured concentrations and snow reflectance (Tanikawa et al. 2002).

Organic materials in the snow may have more distinctive spectral features than aerosols or dust (Takeuchi 2002). Because snow algae (*Chlamydomonas nivalis*) can reproduce in the snow, they cause albedo to decrease in the melt season. Their distinctive reddish hue, caused by carotenoid absorption in the wavelength range from 0.4–0.58 μm and chlorophyll a and b absorption from 0.6–0.7 μm, allows measurement of their concentration with hyperspectral data, subject to their highly variable spatial distribution (Painter et al. 2001).

Adding to the general problem of remote sensing of snow under forest canopies is the reduction of snow albedo by forest litter. The albedo decrease is a significant factor in the energy balance of the snowpack in the forest, where net radiation is the dominant term in the energy balance (Hardy et al. 1998, Melloh et al. 2001). Remotely sensing snow extent and albedo in forested regions remains a challenging research problem.

Snow Temperature

While not uniform, the infrared emissivity of snow is known well enough to compensate for its effects in remote sensing of snow surface temperature. Emitted spectral radiance at wavelength λ from a snow surface at thermodynamic temperature T is given by multiplying the spectral emissivity ε_λ by the Planck function. The

brightness temperature $T_B(\lambda)$, at a given wavelength, temperature, and emissivity, is the temperature of a blackbody that emits the same amount of radiation at that wavelength:

$$\frac{2hc^2}{\lambda^5(e^{hc/k\lambda T_B} - 1)} = \varepsilon_\lambda \frac{2hc^2}{\lambda^5(e^{hc/k\lambda T} - 1)},$$

$$\text{so } T_B = \frac{hc}{k\lambda \ln\left(\dfrac{\varepsilon_\lambda + e^{hc/k\lambda T} - 1}{\varepsilon_\lambda}\right)}, \tag{4}$$

where h is Planck's constant, k is Boltzmann's constant, and c is the speed of light. At near-normal viewing angles, the brightness temperature can be as much as 1.5 K lower than the thermodynamic temperature at wavelengths around 13 μm, based on field-measured spectral emissivity (Figure 9). At the shorter infrared wavelength window, 3.5–4 μm, uncertainty in emissivity does not translate into uncertainty in temperature because of the nonlinear nature of Equation 4, but at longer wavelengths it does. Fortunately, the highest uncertainties in emissivity are beyond the 10.5–12.5 μm atmospheric window.

However, there is a conflict between the published theories of the emissivity of snow. Dozier & Warren (1982), who treat the snow grains as independent scatterers, find that emissivity decreases with grain size, and show a negligible effect of liquid water. Wald (1994) however, proposes a "diffraction-subtraction" model for closely packed snow grains and calculates that snow emissivity decreases with grain size. Moreover, accompanying measurements (Salisbury et al. 1994)
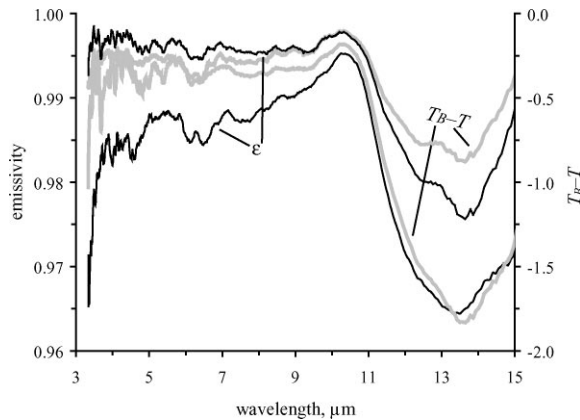
Figure 9 Field measurements of the spectral variability of snow emissivity (Wan & Zhang 1999) and its effect on brightness temperature (T_B) for snow at the melting temperature. The black lines show spectral emissivity, whereas the gray lines show the spectral variability in the difference between temperature and brightness temperature.

show a decrease in emissivity in the presence of liquid water. The only known field measurements of snow emissivity at fine spectral resolution (Wan & Zhang 1999) were not complemented by detailed characterization of the snow.

Land-surface temperature is one of the standard products from MODIS (Wan & Dozier 1996, Wan & Li 1997), and the NASA/EOS algorithm includes snow in its surface classification (Snyder et al. 1998). However, measurements of snow surface temperature have been routinely used in only a few climate or hydrologic studies. Stroeve & Steffen (1998) showed that AVHRR-derived surface temperatures in Greenland were accurate within 1K during summer, less so in winter because of problems with cloud identification. Their results showed that surface temperature of the Greenland ice sheet is strongly dominated by topography, with minimum surface temperatures associated with the high elevation regions. Large interannual variability in surface temperatures occurs during winter associated with katabatic storm events. In their use of infrared temperature measurements to study katabatic winds in Antarctica, King et al. (1998) showed that surface temperatures over a coastal ice shelf are significantly lower than those observed on the lower part of the adjoining coastal slopes as a result of the strong surface temperature inversion that forms over the ice shelf. At the drainage-basin scale, Fily et al. (1999) compared energy balance model results with snow temperatures measured from the Landsat TM and found that areas of topographic shadowing significantly lowered surface temperatures. Marks & Winstral (2001) considered snow-surface temperature in analyzing the disparity in energy and mass fluxes during the snow accumulation and ablation cycle between two proximal sites, illustrating the importance of understanding and spatially accounting for variable energy inputs and snow deposition patterns.

EFFECTS OF THE ATMOSPHERE

Retrieval of Apparent Surface Reflectance

Analyses of remotely sensed data can use either top-of-atmosphere reflectance or apparent surface reflectance spectra ($R_{S,\lambda}$), which is the ratio of the radiance L measured at the sensor to the hypothetical radiance from a completely reflecting Lambertian target given the same irradiance on a level surface under the atmospheric conditions and solar geometry at the time of the acquisition. Atmospheric correction of most Landsat TM or AVHRR data usually requires ancillary information because the instrument does not have channels to retrieve atmospheric water vapor (Liang et al. 2001). MODIS, however, has a water vapor channel, so a self-supporting atmospheric correction algorithm is possible (Vermote et al. 2002). Hyperspectral data also contain enough information themselves to characterize the atmosphere. For example, with AVIRIS data the largest atmospheric effect is caused by water vapor. A nonlinear least-squares water vapor fitting model, which incorporates the atmospheric transmission model MODTRAN4 (Berk et al. 1998), accounts for atmospheric spatial heterogeneity by solving for the atmospheric

conditions pixel by pixel from the AVIRIS radiance data and computes $R_{S,\lambda}$ (Green 2001):

$$R_{S,\lambda} = \left(\frac{\mu_0 E_{0,\lambda} T_{d,\lambda} T_{u,\lambda}}{\pi L_{AVIRIS,\lambda} - \mu_0 E_{0,\lambda} R_{a,\lambda}} + S_\lambda \right)^{-1}. \tag{5}$$

E_0 is the exoatmospheric solar irradiance, T_d is the downward direct and diffuse transmittance of the atmosphere, T_u is the upward atmospheric transmittance to AVIRIS, $L_{AVIRIS,\lambda}$ is the total upwelling spectral radiance at AVIRIS, R_a is the upward reflectance of the atmosphere, and S is its downward reflectance.

Atmospheric Effects in Empirical Models

In general, one would expect that analyses applied to atmospherically corrected data would be superior to the same analyses applied to raw data, but this may not be the case if the algorithm was developed from raw data. Figure 10 compares snow-covered areas derived from high-resolution (1–4 m) photos with those estimated by the standard MODIS algorithm, using 67 MODIS scenes synthesized from AVIRIS data. Each point in the plot represents the snow-covered area in an AVIRIS scene, approximately 120 km^2 each. The snow cover derived from atmospherically corrected images has an overall error of 18.5% and a maximum error of 48.6%. The snow cover derived from the MODIS planetary reflectance without atmospheric correction has an overall error of 12.2% with a maximum error of 31.6%. In both cases, the MODIS algorithm performed well when the snow cover was small. At larger values, however, the algorithm overestimates snow cover. Moreover, the algorithm performance is better with planetary reflectance data than with data that are atmospherically corrected because the MODIS snow-mapping algorithm was developed from TM data without atmospheric correction. The surface reflectance of a dim target is smaller than its planetary reflectance, but the surface reflectance of a bright target is larger than its planetary reflectance. Therefore, the atmospheric correction increases the value of the NDSI, defined by Equation 2, and increases the estimate of the snow cover.

ANISOTROPIC REFLECTANCE

A smooth snow surface has a reflectance peak in the forward direction, because of the forward scattering by the grains, and this peak accounts for a greater fraction of the reflectance in the near-infrared wavelengths where snow is more absorptive because the light emerging from the snowpack is likely to have undergone fewer scattering events (Mishchenko 1994, Leroux et al. 1999, Mishchenko et al. 1999, Nolin & Liang 2000). Where the snow surface is rough, however, either because of sastrugi or suncups, the reflectance peak may be in the backward direction because of shadowing by these large roughness features (Warren et al. 1998, Mondet & Fily 1999). Jin & Simpson (1999, 2000) developed a correction for AVHRR imagery
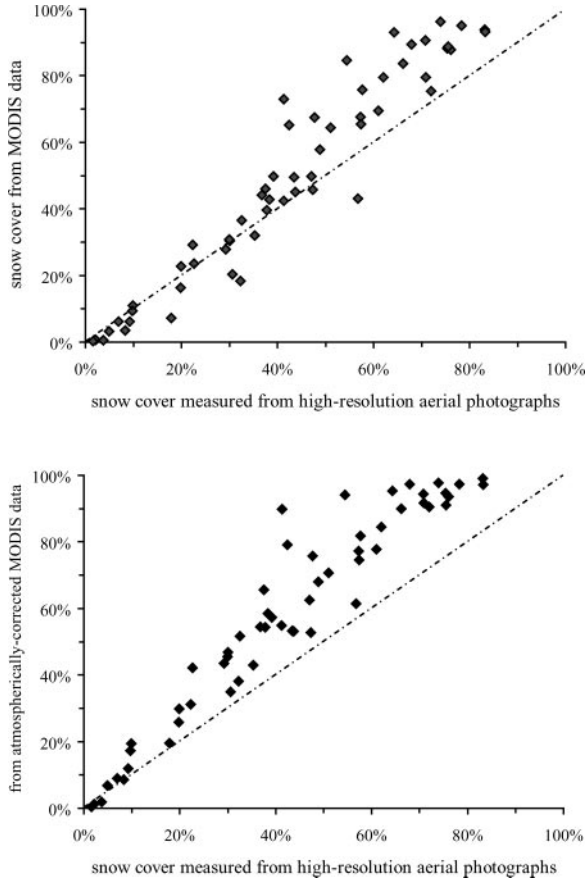
Figure 10 Comparison of high-resolution snow cover derived from aerial photography with that from synthesized MODIS data, without (*top*) and with (*bottom*) atmospheric correction (J. Shi, personal communication).

over sea ice, a flat surface, by incorporating grain-scale and surface-roughness scattering.

Over mountainous terrain, the effects of topography, solar and satellite-viewing geometry, and anisotropic reflectance are mixed together. Moreover, because accurate topographic data for most of Earth are only recently available from the Shuttle Radar Topography Mission (van Zyl 2001), analyses of remotely sensed data that incorporated the topography generally were not able to accurately calculate local illumination or viewing geometry (Konig et al. 2001). Generally, with near-nadir viewing sensors, one might be able to neglect anisotropic reflectance. Although surface roughness (sastrugi, suncups) can affect the bidirectional

reflectance distribution function of snow, Warren et al. (1998) found the effect of sastrugi negligible for near-nadir views. Moreover, they found that sastrugi have little effect on the BRDF (bidirectional reflectance-distribution function) for view angles less than $30°$ in the principal plane and for view zenith angles less than $50°$ at $\lambda = 0.9 \,\mu m$ and solar zenith angle $\theta_0 = 67°$. For smaller zenith angles, the effect would be even smaller. Painter (Painter 2002b) has shown that the variability in the hemispherical-directional reflectance factor for the solar geometry and atmospheric conditions at the time of image acquisition with a near-nadir sensor is negligible, i.e., $R_\lambda(\theta_0, \phi_0, 0, 0) \approx R_\lambda(\theta_0, \phi_0, \theta_r, \phi_r)$ within the small range of angles $[\theta_r, \phi_r]$ observed from the sensor.

FUTURE RESEARCH ISSUES

Applications to date of multispectral and hyperspectral remote sensing of snow-covered area and albedo in alpine terrain have incorporated the following assumptions: (*a*) The variability in the hemispherical-directional reflectance factor for the solar geometry and atmospheric conditions at the time image acquisition is negligible; (*b*) the effects of impurities (dust, soot, and vegetation litter), and the effects of thin snow on snow spectral reflectance are not separable and these effects do not impact retrievals of snow area and grain size; (*c*) linear spectral mixture analysis is valid for hyperspectral scenes of alpine terrain; (*d*) the snow can be characterized by a single effective grain radius, and liquid water in the snow does not affect the retrievals of snow-covered area and grain size; (*e*) effects of surface roughness on the bidirectional reflectance of snow for view geometries over rough terrain are negligible; (*f*) the vegetation canopy is snow-free; and (*g*) for remote sensing of snow temperature, spectral emissivity is known, at least within the atmospheric water vapor windows.

Angular Variability in Reflectance

Painter (2002b) investigates the first assumption (*a*) and shows that retrievals of snow area and grain size are not sensitive to angular variability caused by the AVIRIS scanning range and the topography. However, future spaceborne imaging spectrometers will have larger view angles and will image regions under larger solar zenith angles. Moreover, we still lack a complete dataset of the bidirectional reflectance-distribution function of snow through the wavelength range 0.4–2.5 μm, so there is a lack of validation of the radiative transfer model calculations. In particular, the effects of grain shape are not established.

Effects of Impurities and Thin Snow

Many of the techniques for analyzing hyperspectral data use information about the shape of the spectrum, normalized by mean amplitude. For some kinds of analysis, including those addressing assumption (*b*), however, the absolute value

of the reflectance at some wavelengths is needed, which in turn requires that the local solar illumination and viewing angles are known. Over most of Earth, including the United States, the available topographic data have not been accurate enough to instill any confidence in the calculation of these angles. Now, however, the problem can perhaps be addressed with new digital elevation data from the Shuttle Radar Topography Mission (van Zyl 2001) when those data are available in corrected form; robust incorporation of impure/thin snow endmembers will facilitate the discrimination of dirty/shallow snow from shaded slopes that have similar spectral signatures. Although the aerosol optical depths were small in the investigations where grain size and snow-covered area was retrieved, other snow-covered regions have more turbid atmospheres. Stroeve et al. (1997) found that small amounts of unaccounted-for aerosol may lead to erroneous retrieved reflectance. Further research should explore the sensitivity of hyperspectral analyses to errors in atmospheric correction.

Effect of Vegetation

Assumption (*c*) has been validated in areas where trees are absent or sparse (Nolin et al. 1993, Rosenthal & Dozier 1996, Painter et al. 1998). However, we know that vegetated regions exhibit nonlinear mixing (Roberts et al. 1993, Ray & Murray 1996) so nonlinear mixture analysis may become necessary as canopy density increases. Painter et al. (2003), using an airborne spectrometer, mapped vegetated regions as having larger grain radii than vegetation-free regions, with areas with greater vegetation density showing larger grains. Errors in the retrieved grain sizes may result from shading of the snow substrate with increasing canopy density. A more complete treatment might use a hybrid geometric optics/radiative transfer model (e.g., Ni et al. 1999) to determine the relative spectral fractions of directly illuminated snow, directly illuminated vegetation, and vegetation-shaded snow. Another possibility is that the combined effects of absorption by liquid water in the vegetation and vegetation shading of the snow cover are confounding the spectroscopic analysis.

Effective Grain Size and Liquid Water Content

Assumption (*d*) is often invalid because the penetration depths of different wavelengths vary according to the transparency of ice, so near-surface variability of grain size causes confusing results (Zhou et al. 2004). Green et al. (2002) examine the sensitivities associated with liquid water; because hyperspectral analyses to date have incorporated many bands in the visible and near-infrared spectrum, retrievals should be insensitive to the subtle shifts in the shape of the reflectance spectrum that result from liquid water in the snow. Related problems are that the investigations of liquid water have not validated the results with field observations of the water content of the near-surface layers, and the radiative transfer modeling of snow has not extended into a rigorous treatment of the scattering behavior of a mixture of water and ice.

Effects of Surface Roughness

Over flat terrain, Warren et al. (1998) showed that the effect of anisotropic re-
flectance was negligible for near-nadir observations, but at large scan angles the
imagery must be corrected for anisotropy (Jin & Simpson 1999, 2000, 2001).
Therefore, assumption (*e*) is probably valid for near-nadir but not for off-nadir
sensors. A problem is separating the effects of anisotropic scattering caused at the
grain scale (micrometers to millimeters) from that at the surface-roughness scale
(centimeters to meters).

Snow in the Vegetation Canopy

Assumption (*f*) will often be invalid because coniferous canopies can hold suf-
ficient depths of snow to create an optically thick layer of snow and render the
spectral reflectance closer to that of snow than vegetation. This change in spectral
reflectance will result in inflated measures of subpixel snow area and a lower esti-
mate of grain size. Because of the inherent reflectance and textural variability with
varying interception of snow by the canopy, a temporal analysis of the continuity of
the mapped canopy closure with multiple scenes is probably better than an explicit
radiative transfer treatment. In some cold climates, snow persists in the canopy for
weeks, and the satellite will continue to interpret reflectance from the snow in the
trees. In warmer climates, the snow in the canopy often falls soon after a storm.

Remote Sensing of Snow Temperature

Assumption (*g*) has not been validated through comparison of remotely sensed with
field-measured temperatures, and the discrepancies between competing theories
of emissivity (Dozier & Warren 1982, Wald 1994) have not been resolved by the
available measurements (Wan & Zhang 1999).

Adaptation of Hyperspectral Algorithms to Multispectral Sensors

Another challenge is the application of hyperspectral methods to multispectral
sensors, which likely will always have larger swaths, higher duty cycles, and a
greater commitment to operational stability. The analyses would apply to data from
spectroradiometers that have bands that are sensitive to grain size. The MODIS
band centered at 1.24 μm might prove sensitive enough to map subpixel snow
area and grain size. However, a spectrometer will likely have less sensitivity to
individual band noise. Furthermore, MODIS's 0.5–1.0 km footprint increases the
likelihood of spatial mixing hurdles such as multiple slopes and aspects, discrete
surface grain sizes, or vegetation types within a pixel.

Operational Processing for the Continental or Global Scale

Finally, spectral mixture analysis has been demonstrated to reveal more accurate,
detailed information about snow, but the computer processing requirements for

the matrix inversions or least-squares solutions may be too much for operational data centers to handle. One way through this problem is through simplification of algorithms, for example, the simple two-band method of Kaufman et al. (2002b) or the regression trees of Rosenthal & Dozier (1996). Another possibility is better organization of the processing to take advantage of the increasing capability of inexpensive computers and commercially available database software (Stonebraker et al. 1993, National Research Council 2003).

ACKNOWLEDGMENTS

**The *Annual Review of Earth and Planetary Science* is online at
http://earth.annualreviews.org**

LITERATURE CITED

Adams JB, Smith MO, Gillespie AR. 1993. Imaging spectroscopy: interpretation based on spectral mixture analysis. In *Remote Geochemical Analysis: Elemental and Mineralogical Composition*, ed. CM Pieters, PAJ Englert, pp. 145–66. New York: Cambridge Univ. Press

Aoki T, Fukabori M, Hachikubo A, Tachibana Y, Nishio F. 2000. Effects of snow physical parameters on spectral albedo and bidirectional reflectance of snow surface. *J. Geophys. Res. Atmos.* 105:10219–36

Bass DS, Herkenhoff KE, Paige DA. 2000. Variability of Mars' north polar water ice cap—I. Analysis of Mariner 9 and Viking Orbiter imaging data. *Icarus* 144:382–96

Berk A, Bernstein LS, Anderson GP, Acharya PK, Robertson DC, et al. 1998. MODTRAN cloud and multiple scattering upgrades with application to AVIRIS. *Remote Sens. Environ.* 65:367–75

Bourdelles B, Fily M. 1993. Snow grain-size determination from Landsat imagery over Terre Adélie, Antarctica. *Ann. Glaciol.* 17:86–92

Chen C, Nijssen B, Guo JJ, Tsang L, Wood AW, et al. 2001. Passive microwave remote sensing of snow constrained by hydrological simulations. *IEEE Trans. Geosci. Remote Sens.* 39:1744–56

Chu DA, Kaufman YJ, Ichoku C, Remer LA, Tanre D, Holben BN. 2002. Validation of MODIS aerosol optical depth retrieval over land. *Geophys. Res. Lett.* 29:DOI:10.1029/2001GL013205

Cline DW, Bales RC, Dozier J. 1998. Estimating the spatial distribution of snow in mountain basins using remote sensing and energy balance modeling. *Water Resour. Res.* 34:1275–85

CNES POLDER Team. 2003a. *POLDER Atmosphere, Land and Ocean Mission.* http://smsc.cnes.fr/POLDER/

CNES POLDER Team. 2003b. *POLDER Technical Features.* http://smsc.cnes.fr/POLDER/GP_instrument.htm

Colbeck SC. 1979. Grain clusters in wet snow. *J. Colloid Interface Sci.* 72:371–84

Colee MT, Painter TH, Rosenthal W, Dozier J. 2000. A spatially distributed physical snowmelt model in an alpine catchment. *Proc. West. Snow Conf.* 68:99–102

Daly SF, Davis R, Ochs E, Pangburn T. 2000. An approach to spatially distributed snow modelling of the Sacramento and San Joaquin basins, California. *Hydrol. Process.* 14:3257–71

Davis RE, Jordan RE, Daly S, Koenig GG. 2001. Validation of snow models. In *Model Validation: Perspectives in Hydrological*

Science, ed. MG Anderson, PD Bates, pp. 261–92. New York: Wiley

Dozier J. 1989. Spectral signature of alpine snow cover from the Landsat Thematic Mapper. *Remote Sens. Environ.* 28:9–22 DOI:10.1016/0034-4257(89)90101-6

Dozier J, Davis RE, Perla R. 1987. On the objective analysis of snow microstructure. In *Avalanche Formation, Movement and Effects,* ed. B Salm, H Gubler, pp. 49–59. Wallingford, UK: Int. Assoc. Hydrol. Sci. Publ. No. 162

Dozier J, Frew J. 1990. Rapid calculation of terrain parameters for radiation modeling from digital elevation data. *IEEE Trans. Geosci. Remote Sens.* 28:963–69

Dozier J, Marks D. 1987. Snow mapping and classification from Landsat Thematic Mapper data. *Ann. Glaciol.* 9:97–103

Dozier J, Schneider SR, McGinnis Jr DF. 1981. Effect of grain size and snowpack water equivalence on visible and near-infrared satellite observations of snow. *Water Resour. Res.* 17:1213–21

Dozier J, Warren SG. 1982. Effect of viewing angle on the infrared brightness temperature of snow. *Water Resour. Res.* 18:1424–34

Fily M, Bourdelles B, Dedieu JP, Sergent C. 1997. Comparison of in situ and Landsat Thematic Mapper derived snow grain characteristics in the Alps. *Remote Sens. Environ.* 59:452–60

Fily M, Dedieu JP, Durand Y. 1999. Comparison between the results of a snow metamorphism model and remote sensing derived snow parameters in the Alps. *Remote Sens. Environ.* 68:254–63

Foster JL, Chang ATC, Hall DK. 1997. Comparison of snow mass estimates from prototype passive microwave snow algorithm, a revised algorithm and a snow depth climatology. *Remote Sens. Environ.* 62:132–42

Gillespie AR, Smith MO, Adams JB, Willis SC, Fischer III AF, Sabol DE. 1990. Interpretation of residual images: spectral mixture analysis of AVIRIS images, Owens Valley, California. In *Second Airborne Visible/Infrared Imaging Spectrom. (AVIRIS) Workshop*, pp. 90–54, 243–70. Pasadena, CA: Jet Propulsion Lab.

Golub GH, Van Loan CF. 1996. *Matrix Computations*. Baltimore: Johns Hopkins Univ. Press. 694 pp.

Goodison B, Walker A. 1994. Canadian development and use of snow cover information from passive microwave satellite data. In *Passive Microwave Remote Sensing of Land-Atmosphere Interactions*, ed. B Choudhury, Y Kerr, E Njoku, P Pampaloni, pp. 245–62. Utrecht: VSB

Green RO. 2001. Atmospheric water vapor sensitivity and compensation requirement for Earth-looking imaging spectrometers in the solar-reflected spectrum. *J. Geophys. Res. Atmos.* 106:17443–52

Green RO. 2003. *Understanding the three phases of water with imaging spectroscopy in the solar reflected energy spectrum*. PhD thesis. Univ. Calif., Santa Barbara. 215 pp.

Green RO, Dozier J, Roberts DA, Painter TH. 2002. Spectral snow reflectance models for grain size and liquid water fraction in melting snow for the solar reflected spectrum. *Ann. Glaciol.* 34:71–73

Green RO, Eastwood ML, Sarture CM, Chrien TG, Aronsson M, et al. 1998. Imaging spectroscopy and the airborne visible/infrared imaging spectrometer. *Remote Sens. Environ.* 65:227–48

Grenfell TC, Warren SG. 1999. Representation of a nonspherical ice particle by a collection of independent spheres for scattering and absorption of radiation. *J. Geophys. Res. Atmos.* 104:31697–709

Greuell W, Reijmer CH, Oerlemans J. 2002. Narrowband-to-broadband albedo conversion for glacier ice and snow based on aircraft and near-surface measurements. *Remote Sens. Environ.* 82:48–63 DOI:10.1016/S0034-4257(02)00024-X

Hall DK, Casey KA. 2003. *The MODIS Snow/Ice Global Mapping Project*. http://modis-snow-ice.gsfc.nasa.gov/modis.html

Hall DK, Foster JL, Chang ATC. 1992. Reflectance of snow as measured in situ and from space in sub-Arctic areas in Canada and

Alaska. *IEEE Trans. Geosci. Remote Sens.* 30:634–37

Hall DK, Martinec J. 1985. *Remote Sensing of Ice and Snow*. New York: Chapman Hall. 189 pp.

Hall DK, Riggs GA, Salomonson VV. 1995. Development of methods for mapping global snow cover using moderate resolution imaging spectroradiometer data. *Remote Sens. Environ.* 54:127–40

Hall DK, Riggs GA, Salomonson VV, DiGiromamo N, Bayr KJ. 2002. MODIS snow-cover products. *Remote Sens. Environ.* 83:181–94   DOI:10.1016/S0034-4257(02) 00095-0

Hansen GB. 1999. Control of the radiative behavior of the Martian polar caps by surface CO_2 ice: evidence from Mars Global Surveyor measurements. *J. Geophy. Res. Planets* 104:16471–86

Hardy JP, Davis RE, Jordan R, Ni W, Woodcock CE. 1998. Snow ablation modelling in a mature aspen stand of the boreal forest. *Hydrol. Process.* 12:1763–78

Jin YF, Schaaf CB, Gao F, Li XW, Strahler AH, Zeng XB. 2002. How does snow impact the albedo of vegetated land surfaces as analyzed with MODIS data? *Geophys. Res. Lett.* 29:DOI:10.1029/2001GL014132

Jin ZH, Simpson JJ. 1999. Bidirectional anisotropic reflectance of snow and sea ice in AVHRR Channel 1 and 2 spectral regions—part I: theoretical analysis. *IEEE Trans. Geosci. Remote Sens.* 37:543–54

Jin ZH, Simpson JJ. 2000. Bidirectional anisotropic reflectance of snow and sea ice in AVHRR channel 1 and channel 2 spectral regions—part II: correction applied to imagery of snow on sea ice. *IEEE Trans. Geosci. Remote Sens.* 38:999–1015

Jin ZH, Simpson JJ. 2001. Anisotropic reflectance of snow observed from space over the arctic and its effect on solar energy balance. *Remote Sens. Environ.* 75:63–75

JPL ASTER Team. 2003. *ASTER Instrument Characteristics*.   http://asterweb.jpl.nasa. gov/instrument/character.htm

JPL AVIRIS Team. 2003. *AVIRIS: Airborne Visible/Infrared Imaging Spectrometer*. http://makalu.jpl.nasa.gov/

JPL MISR Team. 2003. *MISR: Multi-angle Imaging SpectroRadiometer*. http://www-misr.jpl.nasa.gov/

Kaab A. 2002. Monitoring high-mountain terrain deformation from repeated air- and spaceborne optical data: examples using digital aerial imagery and ASTER data. *ISPRS J. Photogramm. Remote Sens.* 57:39–52

Kaufman YJ, Gobron N, Pinty B, Widlowski JL, Verstraete MM. 2002a. Relationship between surface reflectance in the visible and mid-IR used in MODIS aerosol algorithm—theory. *Geophys. Res. Lett.* 29:DOI:10.1029/2001GL014492

Kaufman YJ, Kleidman RG, Hall DK, Martins JV, Barton JS. 2002b. Remote sensing of subpixel snow cover using 0.66 and 2.1 μm channels. *Geophys. Res. Lett.* 29:DOI:10.1029/2001GL013580

King JC, Varley MJ, Lachlan-Cope TA. 1998. Using satellite thermal infrared imagery to study boundary layer structure in an Antarctic katabatic wind region. *Int. J. Remote Sens.* 19:3335–48

Kirnbauer R, Blöschl G, Gutknecht D. 1994. Entering the era of distributed snow models. *Nord. Hydrol.* 25:1–24

Klein AG, Hall DK, Riggs GA. 1998. Improving snow cover mapping in forests through the use of a canopy reflectance model. *Hydrol. Process.* 12:1723–44

Klein AG, Isacks BL. 1999. Spectral mixture analysis of Landsat Thematic Mapper images applied to the detection of the transient snowline on tropical Andean glaciers. *Global Planet. Change* 22:139–54

Klein AG, Stroeve J. 2002. Development and validation of a snow albedo algorithm for the MODIS instrument. *Ann. Glaciol.* 34:45–52

Konig M, Winther JG, Isaksson E. 2001. Measuring snow and glacier ice properties from satellite. *Rev. Geophys.* 39:1–27

Leroux C, Lenoble J, Brogniez G, Hovenier JW, De Haan JF. 1999. A model for the bidirectional polarized reflectance of snow. *J. Quant. Spec. Rad. Trans.* 61:273–85

Li W, Stamnes K, Chen BQ, Xiong XZ. 2001. Snow grain size retrieved from near-infrared radiances at multiple wavelengths. *Geophys. Res. Lett.* 28:1699–702

Liang SL, Fang HL, Chen MZ. 2001. Atmospheric correction of landsat ETM+ l and surface imagery—part I: methods. *IEEE Trans. Geosci. Remote Sens.* 39:2490–98

Luce CH, Tarboton DG, Cooley KR. 1998. The influence of the spatial distribution of snow on basin-averaged snowmelt. *Hydrol. Process.* 12:1671–83

Luce CH, Tarboton DG, Cooley KR. 1999. Subgrid parameterization of snow distribution for an energy and mass balance snow cover model. *Hydrol. Process.* 13:1921–33

Marks D, Winstral A. 2001. Comparison of snow deposition, the snow cover energy balance, and snowmelt at two sites in a semiarid mountain basin. *J. Hydrometeorol.* 2:213–27

Martonchik JV, Diner DJ, Crean KA, Bull MA. 2002. Regional aerosol retrieval results from MISR. *IEEE Trans. Geosci. Remote Sens.* 40:1520–31

Martonchik JV, Diner DJ, Kahn RA, Ackerman TP, Verstraete ME, et al. 1998. Techniques for the retrieval of aerosol properties over land and ocean using multiangle imaging. *IEEE Trans. Geosci. Remote Sens.* 36:1212–27

Mätzler C. 1997. Autocorrelation functions of granular media with free arrangement of spheres, spherical shells or ellipsoids. *J. Appl. Phys.* 81:1509–17

Meador WE, Weaver WR. 1980. Two-stream approximations to radiative transfer in planetary atmospheres—a unified description of existing methods and a new improvement. *J. Atmos. Sci.* 37:630–43

Meixner T, Bales RC, Williams MW, Campbell DH, Baron JS. 2000. Stream chemistry modeling of two watersheds in the Front Range, Colorado. *Water Resour. Res.* 36:77–87

Melloh RA, Hardy JP, Davis RE, Robinson PB. 2001. Spectral albedo/reflectance of littered forest snow during the melt season. *Hydrol. Process.* 15:3409–22

Mertes LAK, Smith MO, Adams JB. 1993. Estimating suspended sediment concentrations in surface waters of the Amazon River wetlands from Landsat images. *Remote Sens. Environ.* 43:281–301

Mishchenko MI. 1994. Asymmetry parameters of the phase function for densely packed scattering grains. *J. Quant. Spec. Rad. Trans.* 52:95–110

Mishchenko MI, Dlugach JM, Yanovitskij EG, Zakharova NT. 1999. Bidirectional reflectance of flat, optically thick particulate layers: an efficient radiative transfer solution and applications to snow and soil surfaces. *J. Quant. Spec. Rad. Trans.* 63:409–32

Mondet J, Fily M. 1999. The reflectance of rough snow surfaces in Antarctica from POLDER/ADEOS remote sensing data. *Geophys. Res. Letts.* 26:3477–80

NASA. 1999. *Summary of Landsat Missions and Sensors*. http://landsat.gsfc.nasa.gov/project/Comparison.html

NASA MODIS Team. 2003. *MODIS Technical Specifications*. http://modis.gsfc.nasa.gov/about/specs.html

NASA/GSFC. 2003a. *Aqua*. http://aqua.nasa.gov/

NASA/GSFC. 2003b. *Terra: The EOS Flagship*. http://terra.nasa.gov/

NASA/GSFC EO-1 Team. 2003. *Hyperion Instrument*. http://eo1.gsfc.nasa.gov/Technology/Hyperion.html

National Research Council. 2003. *Government Data Centers: Meeting Increasing Demands*. Washington, DC: Nat. Acad. Press. 56 pp.

Ni W, Woodcock CE, Li X, Strahler AH. 1999. An analytical hybrid GORT model for bidirectional reflectance over discontinuous plant canopies. *IEEE Trans. Geosci. Remote Sens.* 37:987–99

NOAASIS Gateway. 2003. *Advanced Very High Resolution Radiometer—AVHRR*. http://noaasis.noaa.gov/NOAASIS/ml/avhrr.html

Nolin AW. 1998. Mapping the Martian polar ice caps: applications of terrestrial optical remote sensing methods. *J. Geophys. Res. Planets* 103:25851–64

Nolin AW, Dozier J. 2000. A hyperspectral method for remotely sensing the grain size

of snow. *Remote Sens. Environ.* 74:207–16; DOI:10.1016/S0034-4257(00)00111-5

Nolin AW, Dozier J, Mertes LAK. 1993. Mapping alpine snow using a spectral mixture modeling technique. *Ann. Glaciol.* 17:121–24

Nolin AW, Liang S. 2000. Progress in bidirectional reflectance modeling and applications for surface particulate media: snow and soils. *Remote Sens. Rev.* 18:307–42

Nolin AW, Raup B, Scambos T, Stroeve JC. 2001. Mapping snow grain size and albedo on the Greenland ice sheet using an imaging spectrometer. *EOS Trans. AGU* 82:IP22B–0688 (Abstr.)

Nolin AW, Stroeve J. 1997. The changing albedo of the Greenland ice sheet: implications for climate modeling. *Ann. Glaciol.* 25:51–57

Nussenzveig HM, Wiscombe WJ. 1991. Complex angular momentum approximation to hard-core scattering. *Phys. Rev. A* 43:2093–112

O'Brien H, Munis RH. 1975. *Red and near-infrared spectral reflectance of snow. Research Rep. 332*, U.S. Army CRREL, Hanover, NH

Okin GS, Roberts DA, Murray B, Okin WJ. 2001. Practical limits on hyperspectral vegetation discrimination in arid and semiarid environments. *Remote Sens. Environ.* 77:212–25

Painter TH. 2002a. *Cold Land Processes Field Experiment—Hyperion Data.* http://nsidc.org/data/clpx/hyperion.html

Painter TH. 2002b. *The hyperspectral bidirectional reflectance of snow: modeling, measurement, and instrumentation*. PhD thesis. Univ. Calif., Santa Barbara. 279 pp.

Painter TH, Dozier J, Roberts DA, Davis RE, Green RO. 2003. Retrieval of sub-pixel snow-covered area and grain size from imaging spectrometer data. *Remote Sens. Environ.* 85:64–77; DOI:10.1016/S0034-4257(02)00187-6

Painter TH, Duval B, Thomas WH, Mendez M, Heintzelman S, Dozier J. 2001. Detection and quantification of snow algae with an airborne imaging spectrometer. *Appl. Environ. Microbiol.* 67:5267–72

Painter TH, Roberts DA, Green RO, Dozier J. 1998. The effect of grain size on spectral mixture analysis of snow-covered area from AVIRIS data. *Remote Sens. Environ.* 65:320–32; DOI:10.1016/S0034-4257(98)00041-8

Rango A, Itten K. 1976. Satellite potentials in snowcover monitoring and runoff prediction. *Nord. Hydrol.* 7:209–30

Rango A, Martinec J. 1979. Application of a snowmelt-runoff model using Landsat data. *Nord. Hydrol.* 10:225–38

Rango A, Shalaby AI. 1998. Operational applications of remote sensing in hydrology: success, prospects and problems. *Hydrol. Sci. J.* 43:947–68

Raup BH, Kieffer HH, Hare TM, Kargel JS. 2000. Generation of data acquisition requests for the ASTER satellite instrument for monitoring a globally distributed target: glaciers. *IEEE Trans. Geosci. Remote Sens.* 38:1105–12

Ray TW, Murray BC. 1996. Nonlinear spectral mixing in desert vegetation. *Remote Sens. Environ.* 55:59–64

Roberts DA, Gardner M, Church R, Ustin S, Scheer G, Green RO. 1998. Mapping chaparral in the Santa Monica Mountains using multiple endmember spectral mixture models. *Remote Sens. Environ.* 65:267–79

Roberts DA, Smith MO, Adams JB. 1993. Green vegetation, nonphotosynthetic vegetation, and soils in AVIRIS data. *Remote Sens. Environ.* 44:255–69

Rosenthal W, Dozier J. 1996. Automated mapping of montane snow cover at subpixel resolution from the Landsat Thematic Mapper. *Water Resour. Res.* 32:115–30

Sabol DE Jr, Adams JB, Smith MO. 1992. Quantitative subpixel spectral detection of targets in multispectral images. *J. Geophys. Res.* 97:2659–72

Salisbury JW, Daria DM, Wald A. 1994. Measurements of thermal infrared spectral reflectance of frost, snow, and ice. *J. Geophys. Res. Solid Earth* 99:24235–40

Shi J. 1999. An automatic estimation of

snow fraction using ASTER simulated from AVIRIS in alpine regions. In *Proc. Eighth Annu. JPL Airborne Geosci. Workshop*. Pasadena, CA: Jet Propulsion Lab.

Shi J, Dozier J. 1995a. Inferring snow wetness using C-band data from SIR-C's polarimetric synthetic aperture radar. *IEEE Trans. Geosci. Remote Sens.* 33:905–14

Shi J, Dozier J. 1995b. Inferring snow wetness using C-band data from SIR-C's polarimetric synthetic aperture radar (correction). *IEEE Trans. Geosci. Remote Sens.* 33:1340

Shi J, Dozier J. 2000a. Estimation of snow water equivalence using SIR-C/X-SAR, part I: inferring snow density and subsurface properties. *IEEE Trans. Geosci. Remote Sens.* 38:2465–74

Shi J, Dozier J. 2000b. Estimation of snow water equivalence using SIR-C/X-SAR, part II: inferring snow depth and grain size. *IEEE Trans. Geosci. Remote Sens.* 38:2475–88

Snyder WC, Wan Z, Zhang Y, Feng YZ. 1998. Classification-based emissivity for land surface temperature measurement from space. *Int. J. Remote Sens.* 19:2753–74

Stamnes K, Tsay S-C, Wiscombe WJ, Jayaweera K. 1988. Numerically stable algorithm for discrete-ordinate-method radiative transfer in multiple scattering and emitting layered media. *Appl. Opt.* 27:2502–9

Stonebraker M, Frew J, Dozier J. 1993. The Sequoia 2000 project. In *Advances in Spatial Databases*, ed. D Abel, BC Ooi, pp. 397–412. Berlin: Springer-Verlag

Stroeve JC, Nolin AW. 2002. New methods to infer snow albedo from the MISR instrument with applications to the Greenland ice sheet. *IEEE Trans. Geosci. Remote Sens.* 40:1616–25

Stroeve JC, Nolin AW, Steffen K. 1997. Comparison of AVHRR-derived and in situ surface albedo over the Greenland ice sheet. *Remote Sens. Environ.* 62:262–76

Stroeve JC, Steffen K. 1998. Variability of AVHRR-derived clear-sky surface temperature over the Greenland ice sheet. *J. Appl. Meteorol.* 37:23–31

Takeuchi N. 2002. Optical characteristics of cryoconite (surface dust) on glaciers: the relationship between light absorbency and the property of organic matter contained in the cryoconite. *Ann. Glaciol.* 34:409–14

Tanikawa T, Aoki T, Nishio F. 2002. Remote sensing of snow grain size and impurities from airborne multispectral scanner data using a snow bidirectional reflectance distribution function model. *Ann. Glaciol.* 34:74–80

Thomas G, Stamnes K. 1999. *Radiative Transfer in the Atmosphere and Ocean*. Cambridge, UK: Cambridge Univ. Press. 517 pp.

Underwood EE. 1981. *Quantitative Stereology*. Reading, MA: Addison-Wesley. 274 pp.

USGS. 2003. *Advanced Very High Resolution Radiometer (AVHRR)*. http://edc.usgs.gov/products/satellite/avhrr.html

van Zyl JJ. 2001. The shuttle radar topography mission (SRTM): a breakthrough in remote sensing of topography. *Acta Astronaut.* 48:559–65

Vermote EF, El Saleous NZ, Justice CO. 2002. Atmospheric correction of MODIS data in the visible to middle infrared: first results. *Remote Sens. Environ.* 83:97–111; DOI:10.1016/S0034-4257(02)00089-5

Vikhamar D, Solberg R. 2003. Subpixel mapping of snow cover in forests by optical remote sensing. *Remote Sens. Environ.* 84:69–82; DOI:10.1016/S0034-4257(02)00098-6

Wald AE. 1994. Modeling thermal infrared (2–14 μm) reflectance spectra of frost and snow. *J. Geophys. Res. Solid Earth* 99:24241–50

Wan ZM, Dozier J. 1996. A generalized split-window algorithm for retrieving land-surface temperature from space. *IEEE Trans. Geosci. Remote Sens.* 34:892–905

Wan ZM, Li ZL. 1997. A physics-based algorithm for retrieving land-surface emissivity and temperature from EOS/MODIS data. *IEEE Trans. Geosci. Remote Sens.* 35:980–96

Wan ZM, Zhang Y. 1999. *MODIS UCSB Emissivity Library*. http://www.icess.ucsb.edu/modis/EMIS/html/em.html

Warren SG. 1982. Optical properties of snow. *Rev. Geophys. Space Phys.* 20:67–89

Warren SG, Brandt RE, Hinton PO. 1998. Effect of surface roughness on bidirectional reflectance of Antarctic snow. *J. Geophys. Res. Planets* 103:25789–807

Warren SG, Wiscombe WJ. 1980. A model for the spectral albedo of snow, II, snow containing atmospheric aerosols. *J. Atmos. Sci.* 37:2734–45

Williams MR, Melack JM. 1997. Atmospheric deposition, mass balances, and processes regulating streamwater solute concentrations in mixed-conifer catchments of the Sierra Nevada, California. *Biogeochemistry* 37:111–44

Winther JG. 1992. Landsat Thematic Mapper (TM) derived reflectance from a mountainous watershed during the snow melt season. *Nord. Hydrol.* 23:273–90

Winther JG. 1993. Short-term and long-term variability of snow albedo. *Nord. Hydrol.* 24:199–212

Wiscombe WJ. 1980. Improved Mie scattering algorithms. *Appl. Opt.* 19:1505–9

Wiscombe WJ. 1994. *Refractive Index of Water.* ftp://climate.gsfc.nasa.gov/pub/wiscombe/ Refrac_Index/WATER/

Wiscombe WJ. 1995. *Refractive Index of Ice.* ftp://climate.gsfc.nasa.gov/pub/wiscombe/ Refrac_Index/ICE/

Wiscombe WJ, Warren SG. 1980. A model for the spectral albedo of snow, I, pure snow. *J. Atmos. Sci.* 37:2712–33

Wolff EW, Cachier H. 1998. Concentrations and seasonal cycle of black carbon in aerosol at a coastal Antarctic station. *J. Geophys. Res. Atmos.* 103:11033–41

Woo MK, Dubreuil MA. 1985. Empirical relationship between dust content and Arctic snow albedo. *Cold Regions Sci. Technol.* 10:125–32

Zhou X, Li S, Stamnes K. 2004. Effects of vertical inhomogeneity on snow spectral albedo and its implication for optical remote sensing of snow. *J. Geophys. Res.* In press
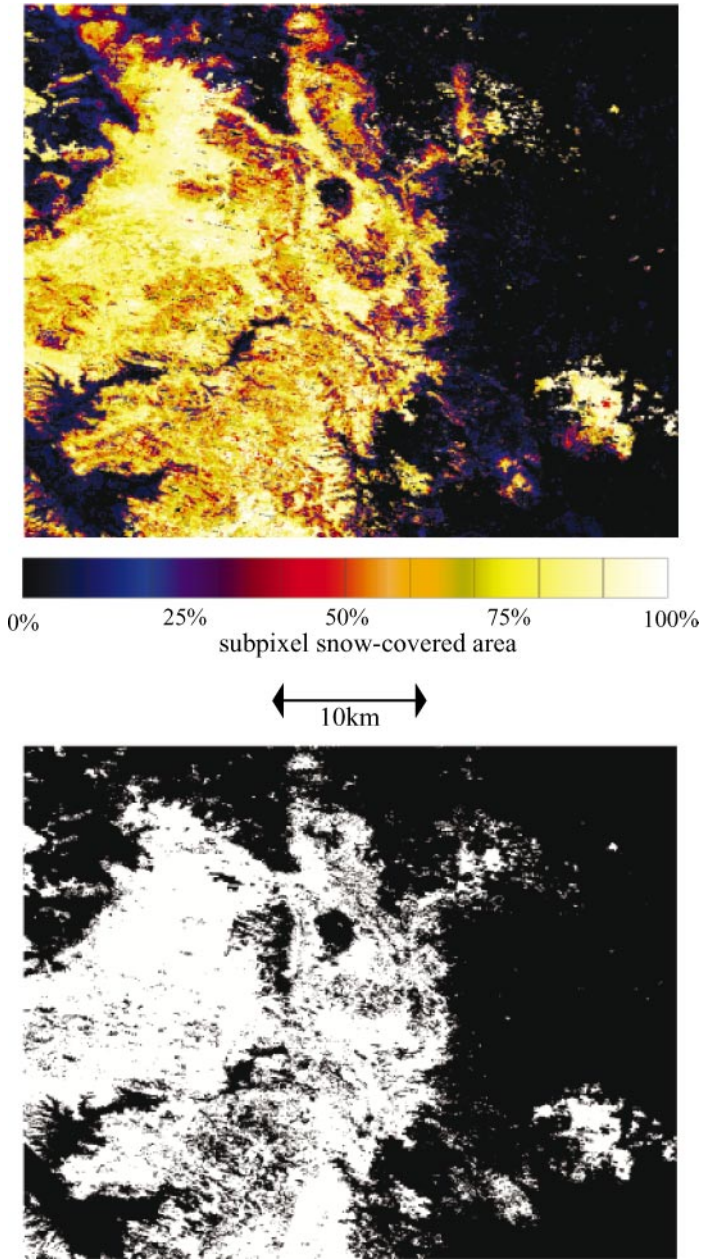
Figure 4 Snow mapping with spectral mixing algorithm (*top*) and MODIS standard algorithm (*bottom*) for NASA's Cold Land Processes field experiment area in the Rocky Mountains. In the standard algorithm, each pixel is mapped as entirely snow or entirely snow-free.

April 5, 1994

March 29, 1996

April 29, 1998

sub-pixel snow-
covered area

1km
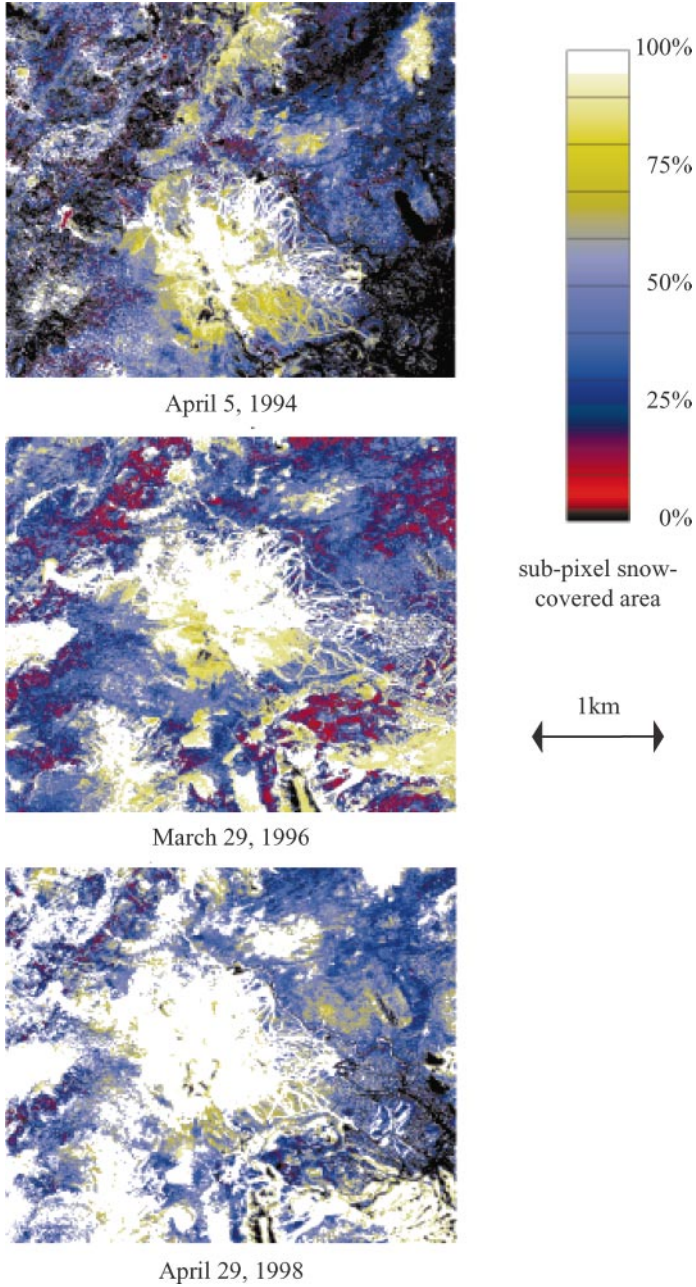
Figure 6 Snow-covered area for three AVIRIS acquisitions near Mammoth Mountain,
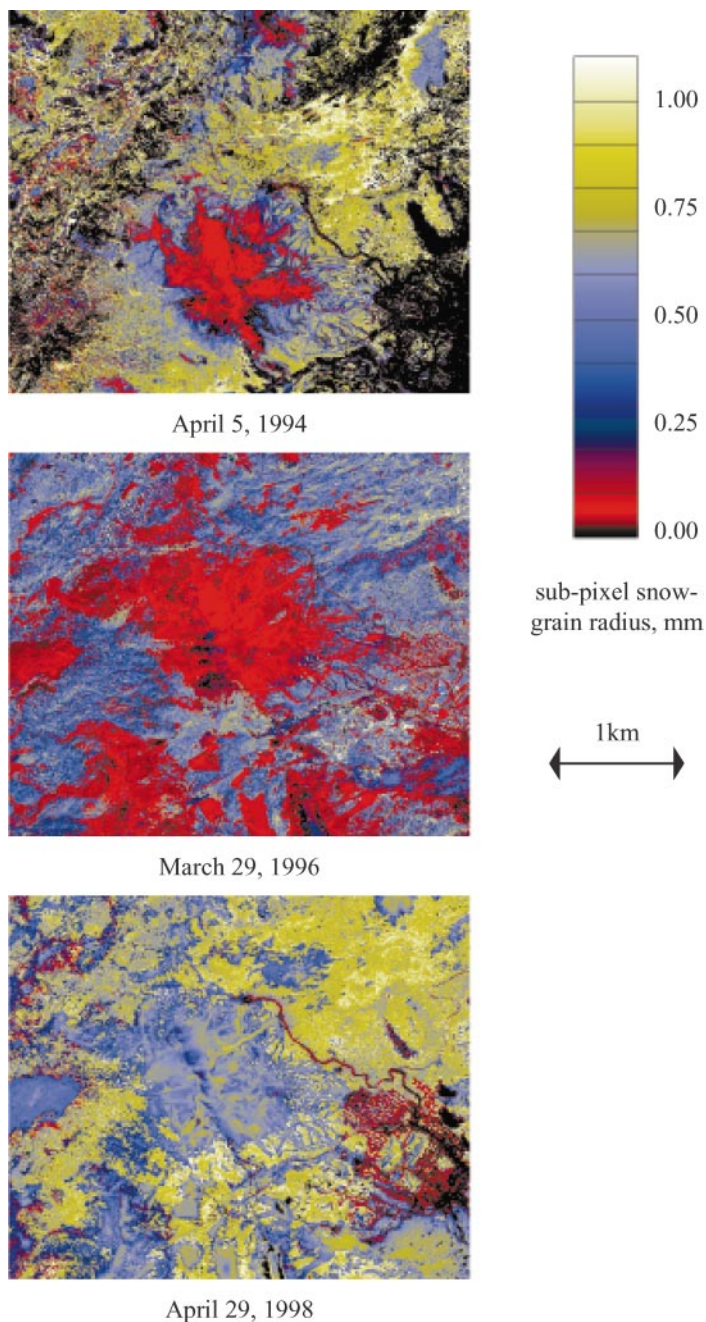Sierra Nevada, for a wide range of snow conditions (Painter et al. 2003).

April 5, 1994

March 29, 1996

April 29, 1998

1.00
0.75
0.50
0.25
0.00

sub-pixel snow-
grain radius, mm

1km

Figure 7 Spatial distribution of optically interpreted mean grain radii for the three
AVIRIS acquisitions in Figure 6.
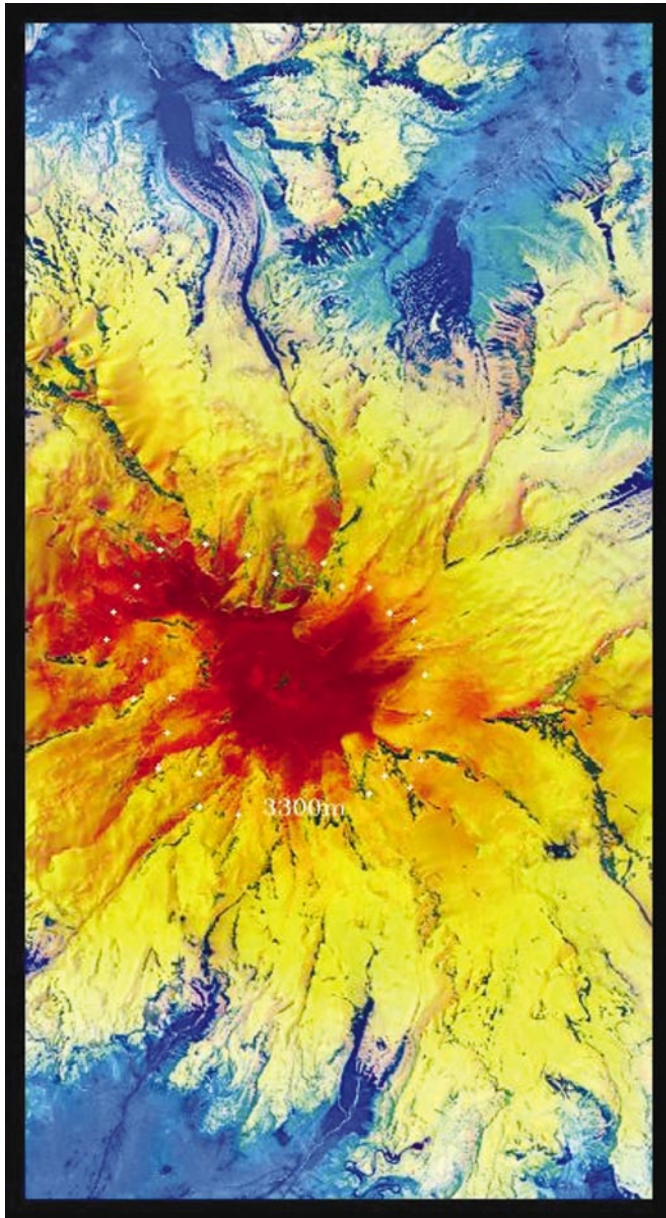
Figure 8   Three phases of water image with water vapor, liquid water, and ice displayed as a false-color image mixing blue, green, and red colors, respectively (Green 2003). Melting snow and ice zones are shown by the color yellow where liquid water and ice are present together. The red colors show areas where the snow is dry and there is little water vapor above the high-altitude surface. Areas largely blue or green are snow-free; any water is either in the atmosphere (vapor) or vegetation (liquid).

CONTENTS